Theoretical and Numerical Studies of Oscillating Airfoils

Ismail H. Tuncer,* James C. Wu,† and C. M. Wang‡
Georgia Institute of Technology, Atlanta, Georgia 30332

Unsteady flowfields around airfoils oscillating in pitch and associated dynamic stall phenomena are investigated. A viscous flow analysis and a simplified vortical flow analysis, both based on an integro-differential formulation of the Navier-Stokes equations are developed and calibrated. The formulation of the viscous flow analysis confines computations only to the viscous flow zone and leads to an efficient zonal solution procedure. In the simplified vortical flow analysis, computational demands are greatly reduced by partial analytic evaluations. Simulated flowfields and computed aerodynamic loads are in good agreement with available experimental data.

Introduction

THE aerodynamic behavior of lifting surfaces undergoing large amplitude pitching motions has been studied by a number of researchers. Until relatively recently, the primary objective of these researchers was to understand the physical processes of unsteady lift generation, in particular those related to the dynamic stall phenomenon observed on retreating helicopter blades. In recent years, there also has been an interest in exploring the large unsteady lift generated during the rapid pitch up to enhance the maneuver capabilities of fighter aircraft.

During the past two decades, the general features of the dynamic stall phenomenon have been established through experimental and semi-empirical investigations.[1-3] The development of a vortex-like disturbance and its passage over an airfoil have been recognized. In 1977, Mehta[4] solved the Navier-Stokes equations for laminar flows to determine the flowfield around an oscillating NACA 0012 airfoil. Although the flowfield was computed in detail, it was limited to low Reynolds number flows and required large amounts of computer time. Carr et al.,[5] McCroskey et al.,[6] and McAlister et al.[7] performed an extensive experimental investigation of unsteady, two-dimensional subsonic flows over oscillating airfoils. In these investigations, it has been pointed out that unsteady flowfields around pitching airfoils experiencing the dynamic stall phenomenon are characterized by massive recirculating regions and numerical simulations can only be achieved by solving the Navier-Stokes equations with a turbulence model.

In a review of the prediction methods for unsteady separated flows and the dynamic stall phenomenon dated before 1980,[8] it has been concluded that the methods then available needed further improvements. Relatively recently, Sankar and Tang[9] and Wu[10] have used the unsteady, compressible, Reynolds-averaged Navier-Stokes equations in the computation of laminar and turbulent flowfields around oscillating airfoils.

It is well known that flowfields associated with massive flow separations are viscous and highly nonlinear. Viscous flow zones, in general, are composed of attached boundary layer zones and detached flow zones that consist of recirculating flows and wakes. The length scales of attached and detached viscous zones are drastically different from each other. The simultaneous existence of these diverse length scales and the diverse flow characteristics in these zones lead to serious theoretical and computational difficulties. However, these difficulties can be removed if several viscous zones coexisting in the flow can be treated individually.

In this study, a method for computing such massively separated unsteady flowfields is developed and calibrated as an extension of a research program continuing since early 1970s.[11-14] This method is based on a velocity-vorticity formulation of the Navier-Stokes equations that consists of the vorticity transport equation and an integral equation for velocity. A two-layer algebraic turbulence model is also incorporated. It is well known that the vorticity field is closely related to the viscous stress, and vorticity is absent in the potential flow zone. Thus, the vorticity transport equation needs only to be solved in the viscous flow zone. In addition, attached boundary layer and detached recirculating flow regions in the viscous flow zone may be treated individually.[12] On the other hand, the integral equation for velocity permits the velocity vector in the viscous flow zone to be evaluated explicitly. This method confines computations into the viscous flow zone only. The confinement of the computations and the zonal approach greatly reduce the computational demands and lead to an efficient zonal solution procedure.

In the absence of recirculating flow zones, the viscous flow zone consists of a thin boundary layer around an airfoil and a wake zone. In these unsteady attached flowfields around pitching airfoils, vorticity is shed into the wake from the trailing edge. In the second part of this study, the vorticity content of the boundary layer is justifiably approximated by a vortex sheet, and the vorticity in the wake is treated as concentrated dosages of vorticity. This simplified vortical flow analysis simulates attached flowfields around pitching airfoils. Important contributors to nonlinear unsteady aerodynamic loads are identified, and their relative importance is determined.

Full Viscous Flow Analysis

The unsteady, incompressible motion of a viscous fluid with negligible body forces is governed by the familiar continuity and the Reynolds-averaged Navier-Stokes equations:

$$\nabla \cdot \boldsymbol{V} = 0 \tag{1}$$

$$\frac{\partial \boldsymbol{V}}{\partial t} + (\boldsymbol{V} \cdot \nabla)\boldsymbol{V} = -\frac{1}{\rho}\nabla p + \nabla \cdot (v_e \nabla \boldsymbol{V}) \tag{2}$$

where $\boldsymbol{V}$ is the velocity, ρ is the density of the fluid, p is the pressure, and v_e is the effective viscosity.

Received Feb. 6, 1989; revision received Dec. 1, 1989.

*Postdoctoral Fellow, School of Aerospace Engineering.
†Professor, School of Aerospace Engineering. Associate Fellow AIAA.
‡Senior Research Engineer, School of Aerospace Engineering.

It is advantageous to employ the concept of vorticity $\boldsymbol{\omega}$ defined by

$$\nabla \times V = \boldsymbol{\omega} \tag{3}$$

Taking the curl of Eq. (2) and using Eq. (3), a vorticity transport equation is obtained. In studying oscillatory motions of solid bodies, it is convenient to formulate the vorticity transport equation in a rotating reference frame attached to the solid body. It reads

$$\frac{\partial \boldsymbol{\omega}}{\partial t} = -(V_R \cdot \nabla_R)\boldsymbol{\omega} + \nabla_R^2(v_e \boldsymbol{\omega}) \tag{4}$$

where the subscript R indicates that the velocity vector and the differentiations are defined in the rotating reference frame. The vorticity transport equation describes the kinetic transport of vorticity. It has been shown in Ref. 11 that all the vorticity in the fluid domain originates from the fluid boundary in contact with a solid. This vorticity spreads into the fluid domain by diffusion and then is transported away from the solid boundary by both convection and diffusion processes. These processes produce a region of nonzero vorticity around the solid body. However, in high Reynolds number flows, a large region of the flow domain is vorticity free, and Eq. (4) needs to be solved only in the region containing vorticity.

Furthermore, in high Reynolds number flows, the vortical region can conveniently be separated into attached and detached flow regions. In the attached flow region, the flow direction is tangential to the solid surface, and the diffusion of vorticity along the flow direction is negligible compared to its convection. In this region, the boundary-layer simplification that neglects the streamwise diffusion of vorticity is justified.

The relationship between the vorticity and velocity fields at any given instant of time, which is described by Eqs. (1) and (3), constitutes the kinematic aspect of the problem. Wu[11] has shown that Eqs. (1) and (3) can be recast into an integral representation for the velocity vector in terms of the vorticity field and the velocity boundary conditions:

$$V(\boldsymbol{r}) = -\frac{1}{2\pi}\int_R \frac{\boldsymbol{\omega}_o \times (\boldsymbol{r}_o - \boldsymbol{r})}{|\boldsymbol{r}_o - \boldsymbol{r}|^2}\,dR_o + \frac{1}{2\pi}\int_B \frac{(V_o \cdot \boldsymbol{n}_o)(\boldsymbol{r}_o - \boldsymbol{r}) - (V_o \times \boldsymbol{n}_o) \times (\boldsymbol{r}_o - \boldsymbol{r})}{|\boldsymbol{r}_o - \boldsymbol{r}|^2}\,dB_o \tag{5}$$

where $\boldsymbol{r}$ is the position vector, the subscript o denotes the variables and the integration in the $\boldsymbol{r}_o$ space, R is the flow domain, B is the boundaries of the flow domain, and $\boldsymbol{n}$ is the unit normal vector on B directed away from the domain R. In particular, the flow domain for the airfoil problem is doubly connected, and B consists of B_s, the solid boundary, and B_∞, the far-field boundary. It should be noted that the far-field boundary conditions are applied analytically at the limit as r_o goes to infinity.

As mentioned, Eq. (4) needs to be solved only in the region containing vorticity. Thus, the velocity values during the numerical solution are needed only in this region. Since the velocity vector at any point in the flowfield can explicitly be evaluated by Eq. (5), computations are conveniently confined only to the vortical flow zone. The vorticity free potential flow zone is excluded from the computations.

Boundary Conditions on Kinetics

Equation (4) is parabolic in time and elliptic in space. At any instance of time, a boundary value problem is solved, and the vorticity values on the inner and outer boundaries need to be prescribed. The outer boundary is taken to be outside the region containing vorticity. However, if the outer boundary cuts through the vortical wake, then the gradient of vorticity in the direction normal to the boundary is assumed to be zero, which allows vortices to pass through the downstream boundary at a local velocity.

The inner boundary is the solid surface B_s, and the vorticity is generated continuously at this surface. In Ref. 15, it has been shown that the solid boundary vorticity values can be determined through the kinematic relationship between the instantaneous velocity and vorticity fields. It should be noted that the kinematic relationship, Eq. (5), is valid in both the solid region S and the fluid region R. Therefore, the vorticity field throughout S and R must be such that the velocity in S as computed by Eq. (5) should agree with the prescribed solid body motion. Equation (5) applied on B_s and the principle of conservation of vorticity give rise to the relations suitable for the evaluation of the surface vorticity distribution:

$$\frac{1}{2\pi}\int_{B_s^+} \frac{\boldsymbol{\omega}_{s_o} \times (\boldsymbol{r}_o - \boldsymbol{r}_s)}{|\boldsymbol{r}_o - \boldsymbol{r}_s|^2}\,dR_o = -V(r_s,t) - \frac{1}{2\pi}\int_{R-B_s^+} \frac{\boldsymbol{\omega}_o \times (\boldsymbol{r}_o - \boldsymbol{r}_s)}{|\boldsymbol{r}_o - \boldsymbol{r}_s|^2}\,dR_o + \frac{1}{2\pi}\int_B \frac{(V_o \cdot \boldsymbol{n}_o)(\boldsymbol{r}_o - \boldsymbol{r}_s) - (V_o \times \boldsymbol{n}_o) \times (\boldsymbol{r}_o - \boldsymbol{r}_s)}{|\boldsymbol{r}_o - \boldsymbol{r}_s|^2}\,dB_o \tag{6}$$

where B_s^+ is a boundary adjacent to B_s where the surface vorticity distribution is evaluated, ω_s is the surface vorticity, and $\boldsymbol{r}_s$ is a point on B_s. With prescribed $V(\boldsymbol{r}_s,t)$ and having evaluated the interior vorticity distribution in $R - B_s^+$, the surface vorticity distribution ω_s can be evaluated through Eq. (6). Note that Eq. (6) is a vector equation, and either component can be used to solve for ω_s.

Turbulence Modeling

A two-layer algebraic eddy viscosity model developed by Baldwin and Lomax[16] is employed in simulating the Reynolds stress. In this model, the closure is simply achieved by replacing the kinematic molecular viscosity v in the momentum equation with the effective viscosity $v_e = v + v_t$, v_t being the kinematic turbulent eddy viscosity coefficient. The model gives the eddy viscosity as follows:

$$v_t = v_{ti} \qquad \text{for } y \le y_{\text{crossover}} \tag{7}$$

$$v_t = v_{to} \qquad \text{for } y \ge y_{\text{crossover}} \tag{8}$$

where the subscripts i and o stand for inner and outer, respectively; $y_{\text{crossover}}$ is the smallest value of y at which eddy viscosity values from the inner and outer formulas are equal; and v_{ti} is based on the Prandtl-Van Driest formulation:

$$v_{ti} = l^2|\omega| \tag{9}$$

where l is the mixing length defined by Prandtl, modified by the Van Driest damping factor.[16]

The eddy viscosity in the outer region v_{to} is given by

$$v_{to} = KC_{cp}F_{\text{wake}}F_{\text{kleb}}(y) \tag{10}$$

where $K = 0.0168$, $C_{cp} = 1.6$, and F_{wake} and $F_{\text{kleb}}(y)$ are functional values based on the vorticity field and some empirical factors.

The values of v_{ti} and v_{to} are evaluated along the secondary grid lines that are perpendicular to the arifoil surface or to the wake centerline. The wake centerline is taken to be the radial grid line emanating from the trailing edge.

Evaluation of Aerodynamic Loads

The evaluation of the aerodynamic lift, drag, and moment coefficients are all based on the proper integration of the pressure coefficient on the airfoil surface. In this study, the pressure is obtained through an integral representation based on the Navier-Stokes equations. The common way of inte-

grating the momentum equation [Eq. (2)] along the airfoil surface has been avoided simply because of the difficulty and poor accuracy experienced in the evaluation of $\partial\omega/\partial n$ on the solid surface. In the formulation of the integral representation for pressure, the vector momentum equation is first expressed in the inertial frame of reference in terms of vorticity as follows:

$$\frac{\partial V}{\partial t} - V \times \omega = -\frac{1}{2}\nabla V^2 - \frac{1}{\rho}\nabla p - \nabla \times (v_e \omega) \tag{11}$$

Furthermore, the total pressure h is defined as

$$h = \frac{p}{\rho} + \frac{V^2}{2} \tag{12}$$

Substituting the preceding equation into Eq. (11) and taking the divergence leads to the following Poisson equation:

$$\nabla^2 h = \nabla \cdot (V \times \omega) \tag{13}$$

Equation (13) then is cast into an integral equation similar to the velocity integral, Eq. (5). Pressure on the airfoil surface is obtained through integration over the velocity and the vorticity fields. Details are given in Ref. 17.

Numerical Formulation

The solution of unsteady flow problems is based on the numerical solution of the discretized governing equations, namely, the vorticity transport equation, Eq. (4), and the integral equation for velocity vector, Eq. (5). The numerical formulation is performed in a transformed complex ζ plane. The following Joukowsky transformation maps a unit circle in ζ plane onto an airfoil profile:

$$z = \zeta + \delta + \frac{c^2}{\zeta + \delta} + \sigma \tag{14}$$

where c^2 and δ are constants related to the airfoil thickness and camber specifications. Equation (14) with $c^2 = 0.8061$ and $\delta = -0.06474$ closely defines the NACA 0012 airfoil profile, and σ determines the location of the origin along the chord in z plane. This origin is placed on the location of the pitching axis. The governing equations are discretized on an O grid. In a (r,θ) cylindrical coordinate system, the grid is uniformly distributed in θ direction and is stretched exponentially in r direction. A sample computational grid in the physical plane is given in Fig. 1.

In discretizing the transformed vorticity transport equation, a first-order backward difference scheme for discretizing the unsteady term, a second upwind differencing scheme for discretizing the convection terms, and a second-order central differencing for discretizing the diffusion terms are used. The numerical solution of the discretized equations is based on the successive line under-relaxation (SLUR) method along radial lines of the O grid. The integral equations for the velocity, surface vorticity, and surface pressure fields are solved by using finite Fourier series expansions of the field variables at each circular ring of the O grid and are partially evaluated analytically.[18] This approach improves the computational efficiency and accuracy considerably.

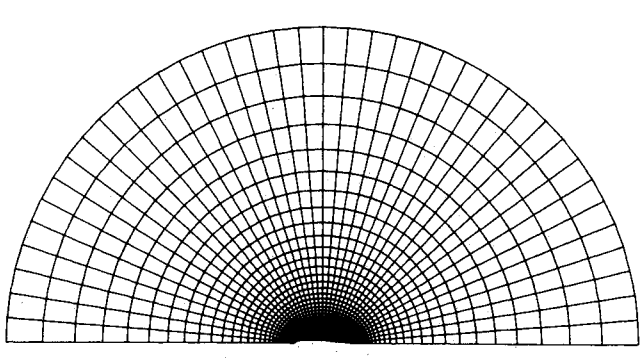

Fig. 1 The O grid in physical plane.

Simplified Vortical Flow Analysis

In the simplified analysis, it is assumed that the viscous flow zone is confined to a thin boundary-layer region around the lifting surface and the wake region trailing it. In high Reynolds number flows, these regions are thin and are justifiably represented by a vortex sheet surrounding the solid body and by vortex filaments in the wake. These approximations, which neglect the diffusion of vorticity, simplify the flow equations and lead to a simple analysis. The conservation of momentum equation states that the vortex filaments in the wake are convected with the local fluid velocity. Solution of the flow problem then reduces to the determination of a vortex sheet strength γ, which represents the integrated vorticity across the boundary layer and the modeling of the vortex shedding process at the trailing edge.

The vortex sheet length distribution is evaluated in a manner similar to the evaluation of the surface vorticity distribution in the viscous flow analysis. In this case, the interior vortical region in Eq. (6), $R - B_s^+$, simply consists of vortex filaments in the wake. Similarly, the component of Eq. (6) associated with the tangential velocity and the conservation of total vorticity equation are solved simultaneously for the vortex sheet strength distribution. For simplicity and convenience in mathematical manipulations, the Joukowsky transformation, Eq. (14), is used. Considerable manipulations[19] in the transformed $\zeta(r,\theta)$ plane lead to the following vortex sheet strength distribution expression for a pitching motion of a Joukowsky airfoil:

$$\gamma_{\zeta\theta_s} = -\Omega\left[C_1 + C_2\left(\frac{1}{\zeta_s} + \zeta_s\right) + C_3\frac{\zeta_s}{(\zeta_s + \delta)(1 + \delta\zeta_s)}\right] - 2U_\infty \sin(\theta - \alpha) - \frac{1}{2\pi}\sum_{k=1}^{n}\Gamma_k \frac{r_k^2 - 1}{1 + r_k^2 - 2r_k\cos(\theta_s - \theta_k)} \tag{15}$$

where

$$C_1 = 1 - \frac{c^2}{\delta^2}$$

$$C_2 = \delta + \sigma + \frac{c^2}{\delta}$$

$$C_3 = \left[\frac{c^2}{\delta^2} - \frac{c^4}{(1-\delta^2)^2}\right](1 - \delta^2)$$

where ζ_s represents the location on the solid boundary $(1,\theta_s)$ in the complex plane, and Γ_k is the magnitude of the kth wake vortex filament that is located at (r_k,θ_k). Note that for noncirculatory flows, in which there is no vorticity in the wake, the noncirculatory vortex sheet strength is given analytically in terms of the pitching velocity and the instant angle of attack α.

Modeling of Vortex Shedding

In this simplified vortical flow analysis, it is assumed that the vorticity in the boundary layers is shed into the wake at the trailing edge. The modeling of the vortex shedding is based on the conservation of momentum and mass in a sufficiently small control volume at the trailing edge. The concept and the related terms are illustrated in Fig. 2.

The boundary-layer edge velocities at the trailing edge, V_l and V_u, are equal to the local vortex sheet strength values. In numerical computations they are evaluated at a point 5%

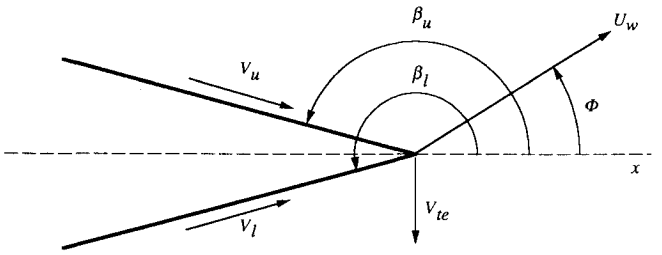

Fig. 2 Modeling of vortex shedding at the trailing edge.

chord length upstream of the trailing edge. The velocity due to the pitching motion is V_{te}. The angle at which the nascent vortex filament leaves the trailing edge, its magnitude, and departure velocity, respectively, are obtained as[19]

$$\tan\phi = \frac{V_l^2 - V_u^2}{V_l^2 + V_u^2}\tan\beta + \frac{(V_u + V_l)V_{te}}{(V_l^2 + V_u^2)\cos\beta} \tag{16}$$

$$\Gamma_w = \frac{1}{2}(V_l^2 - V_u^2)\frac{\cos^2\beta}{\cos^2\phi}\Delta t \tag{17}$$

$$U_w = \frac{1}{2}(V_l + V_u)\frac{\cos\beta}{\cos\phi} \tag{18}$$

where 2β is defined as $\beta_l - \beta_u$, and Δt is the time interval between time steps.

This formulation assumes that the flow does not separate at the trailing edge. In the case of flow separation, the boundary-layer edge velocity on the separated surface is set to zero.

Evaluation of Aerodynamic Forces

A general theory for aerodynamic forces and moments developed by Wu[11] through a rigorous analysis of the Navier-Stokes equations may be written for two-dimensional flows as

$$\boldsymbol{F} = -\rho\frac{\mathrm{d}}{\mathrm{d}t}\int_{R_\infty} \boldsymbol{r}\times\boldsymbol{\omega}\,\mathrm{d}R + \rho\frac{\mathrm{d}}{\mathrm{d}t}\int_{R_s} \boldsymbol{V}\,\mathrm{d}R \tag{19}$$

where R_∞ is the unlimited domain jointly occupied by the fluid and the solid, and R_s is the domain occupied by the solid only. Equation (19) states that the force exerted on a solid body by fluid is related to the time rate of change of the vorticity moment and the inertial force due to solid body motion. In this simplified vortical flow analysis, Eq. (19) may further be simplified by introducing the vortex sheet concept:

$$\boldsymbol{F} = -\rho\frac{\mathrm{d}}{\mathrm{d}t}\int_{B_s} \boldsymbol{r}\times(\boldsymbol{\gamma} - \boldsymbol{V}\times\boldsymbol{n}_s)\,\mathrm{d}B - \rho\frac{\mathrm{d}}{\mathrm{d}t}\int_W \boldsymbol{r}\times\boldsymbol{\omega}\,\mathrm{d}R \tag{20}$$

where $\boldsymbol{n}_s$ is the unit vector normal to the solid surface, and the magnitude of $\boldsymbol{V}\times\boldsymbol{n}_s$ is the component of the surface velocity v_s in the direction tangent to the surface.

In the noncirculatory flows, the first integral term in Eq. (20) can be evaluated analytically by substituting the analytic expression for the noncirculatory vortex sheet strength distribution given in Eq. (15).[19] This noncirculatory aerodynamic force is equivalent to the familiar apparent mass effect. In its component form, it reads

$$F_{x_{nc}} = \rho\pi[\beta\Omega^2\cos\alpha + 4c^2\Omega U_\infty\sin(2\alpha) + \beta\dot{\Omega}\sin\alpha] \tag{21}$$

$$F_{y_{nc}} = \rho\pi[\beta\Omega^2\sin\alpha + 4c^2\Omega U_\infty\cos(2\alpha) + \beta\dot{\Omega}\cos\alpha] \tag{22}$$

where

$$\beta = (1+2c^2)(\delta+\sigma) + \frac{\sigma c^4}{(1-\delta^2)^2} - \frac{2\delta c^4}{1-\delta^2} - \frac{c^6\delta}{(1-\delta^2)^3}$$

and Ω is the angular acceleration.

Fig. 3 Steady-state streamlines: $\alpha = 5$ deg and $Re = 10^6$.

Results and Discussions

The NACA 0012 airfoil oscillating in pitch about its quarter chord has been investigated extensively using both the full viscous flow analysis and the simplified vortical analysis. The oscillatory motion is defined by the time-dependent angle of attack α:

$$\alpha = \alpha_{\min} + \frac{1}{2}(\alpha_{\max} - \alpha_{\min})(1 - \cos\omega t)$$

where $\alpha_{\min}$ and $\alpha_{\max}$ are the minimum and the maximum angles of attack of the oscillatory motion, and ω is the frequency of the motion. Three cases involving dynamic stall are first discussed. In all of these cases, $\alpha_{\min} = 5$ deg, $\alpha_{\max} = 25$ deg, and the Reynolds number, which is based on the chord length and the freestream velocity, is 10^6. The reduced frequency of the oscillatory motion k, which is defined as $k = \omega c/2U_\infty$, is also 0.10, 0.15, and 0.25, respectively. An 80×60 grid with 80 grid points on the airfoil surface is used. The initial transient is computed at $\alpha = 5$ deg, and a steady flowfield is established at a time that corresponds to 6–8 chord length travel of the airfoil. Streamlines for this flowfield are given in Fig. 3. The pitching motion is then introduced, and the unsteady flowfield is solved by marching in time with a constant time step.

In the case $k = 0.15$, the development of the unsteady flowfield is shown in Figs. 4 and 5. During the upstroke ($\uparrow$), as the airfoil reaches the proximity of the static stall angle ($\alpha \cong 12$ deg), the flowfield is still fully attached. Boundary layers on the upper surface, however, grow considerably. As $\alpha \cong 20$ deg $\uparrow$ is approached, a shallow reversed flow region, which initiates at $\alpha \cong 7$ deg $\uparrow$ at the trailing edge, expands upstream rapidly. This flow reversal reaches the leading edge at $\alpha \cong 23$ deg $\uparrow$. An abrupt separation of the boundary layers and the development of the leading-edge vortex is observed between $x/c \cong 0.05$ and 0.25 at $\alpha \cong 23.9$ deg $\uparrow$. In an experimental study[5] conducted with the same motion parameters at $Re = 2.5 \times 10^6$, it is reported that the hot-wire anemometry measurements detect the flow reversal at around $\alpha \cong 19$–20 deg $\uparrow$. This flow reversal then progresses up to $x/c \cong 0.30$. The leading-edge vortex is observed to form at $\alpha \cong 23.4$ deg $\uparrow$ as an abrupt boundary-layer separation.

As the airfoil continues its upstroke, the leading-edge vortex grows. At $\alpha \cong 24.9$ deg $\uparrow$, having already covered the airfoil surface, the vortex bubble is about to burst. Up to this point, the average speed at which the vortex travels is evaluated to be approximately $0.3U_\infty$. During the downstroke ($\downarrow$), as the leading-edge vortex moves off the airfoil and is shed into the wake, the development of a counterclockwise trailing-edge vortex is observed at $\alpha \cong 24.4$ deg $\downarrow$. In the experimental study,[5] the vortex core is observed to pass off the trailing edge at $\alpha \cong 24.8$ deg $\downarrow$, and it travels with a speed of approximately 35–40% of the freestream velocity. In addition, it is also reported that at $\alpha \cong 23.1$ deg $\downarrow$ a second vortex-like disturbance begins to form ahead of midchord and moves downstream.

The shedding of the trailing-edge vortex is observed at $\alpha \cong 22.8$ deg $\downarrow$. Some secondary weak vortex structures subsequently develop. As α decreases, the flow reattachment process starts from the leading edge downward. At $\alpha \cong 9.4$ deg $\downarrow$, the flow on the upper surface attaches completely. Yet, the pressure distribution on the airfoil (Fig. 6) indicates that the

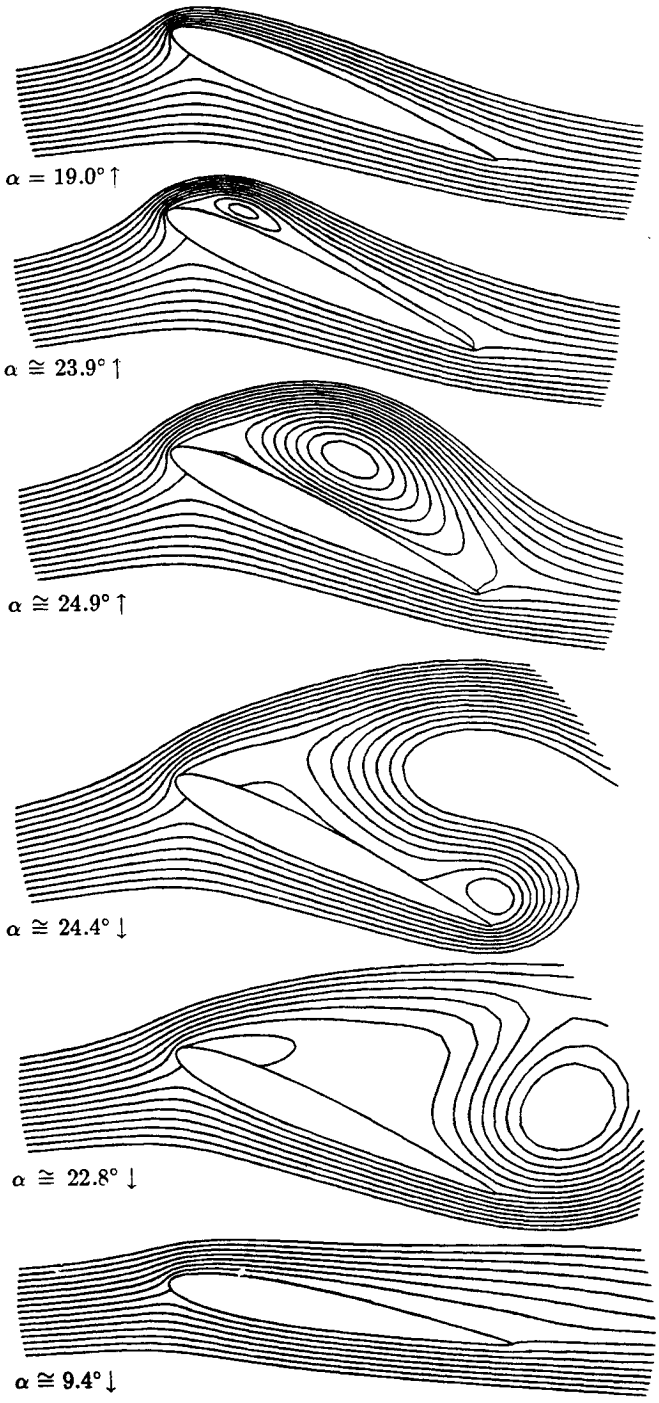

Fig. 4 Instantaneous streamlines: $\alpha_{min} = 5$ deg, $\alpha_{max} = 25$ deg, $Re = 10^6$, and $k = 0.15$.

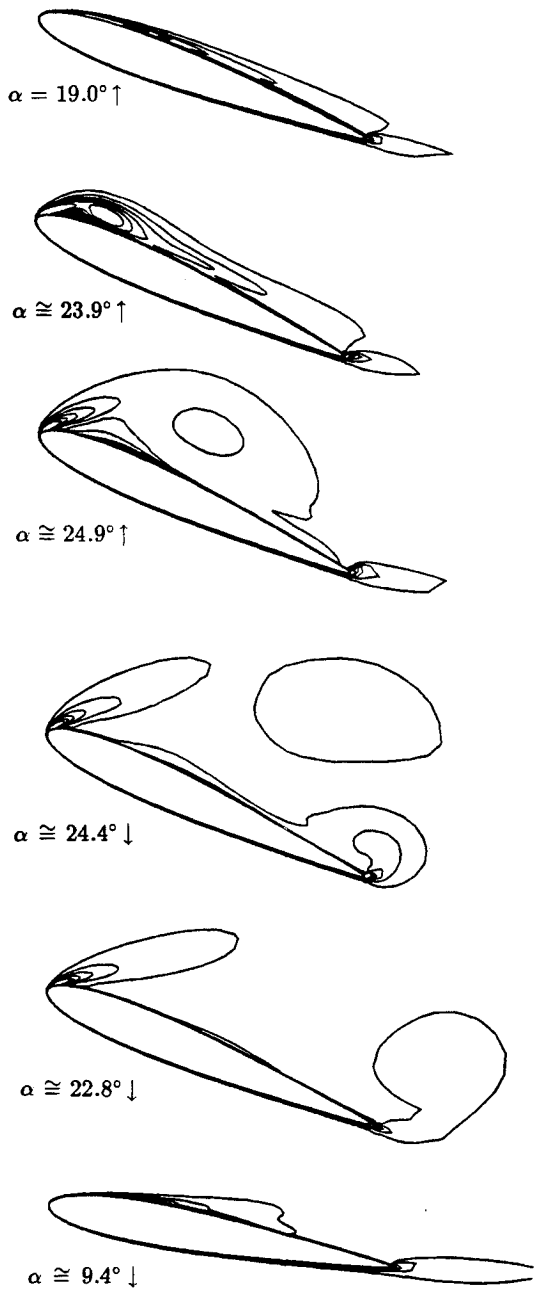

Fig. 5 Instantaneous vorticity contours: $\alpha_{min} = 5$ deg, $\alpha_{max} = 25$ deg, $Re = 10^6$, and $k = 0.15$.

suction on the airfoil has not been recovered. This is attributed to the thick boundary-layer profile aft of $x/c \cong 0.40$. In the experimental study,[5] it is reported that the reattachment process starts at $\alpha \cong 16.5$ deg ↓, and it is completed by $\alpha \cong 7$ deg ↓. It is also observed that although the flow has reattached to the airfoil surface during the downstroke, the rest of the potential flow did not appear to return to unstalled conditions until the airfoil passed through its minimum angle.

The preceding computations were performed on a CDC CYBER 990 computer on its highly optimized scalar mode. It took approximately 5 min of CPU time to reach the steady-state solution and 30 min of CPU time to compute the unsteady flowfield for a complete cycle of the oscillatory motion.

Figure 6 illustrates the time history of the upper surface pressure distribution and its comparison with the experimental data,[7] which are obtained under the following conditions: $k = 0.099$, $\alpha_{min} = 4.86$ deg, $\alpha_{max} = 24.74$, $Re = 0.98 \times 10^6$, and $M_\infty = 0.072$. The time history of the aerodynamic load coefficients is given in Fig. 7. As it is seen, the agreement between the experimental[7] and the computational results is remarkably good. The details of the deep-stall hysteresis loops measured in experiments are captured by the present computations. Quantitative differences do exist but are all within the uncertainty bounds of the experimental study.

During the upstroke, the computed lift coefficient increases linearly until the leading-edge vortex forms. The lift slope is 4.7, which is very close to that of the steady flow. The formation of the leading-edge vortex then causes a steep increase in the lift. At $\alpha \cong 24.9$ deg ↑, as a result of the burst of the bubble at the trailing edge and the shedding of clockwise vorticity, the lift drops drastically. At maximum angle of

attack, the lift coefficient reaches a local minimum. Due to the suction generated by the trailing-edge vortex, it subsequently rises to a second local maximum. This local maximum lift coefficient is higher in the experiments. Besides the experimental uncertainty, the underprediction of the trailing-edge vortex suction in the computations may be attributed to the poor performance of the turbulence model in the wake region.

During the downstroke, following the shedding of the trailing-edge vortex at $\alpha \cong 22.8$ deg ↓, the lift initially decreases rapidly. As the flow reattaches at the trailing edge and as the secondary vortex structures develop, the lift curve flattens. The minimum lift is observed at $\alpha \cong 11$ deg ↓ just before the flow attaches fully on the upper surface. In the experiments, reattachment occurs later and the minimum lift is realized at $\alpha \cong 7$ deg ↓. The early reattachment of the boundary layers in the computed results as compared to the experimental data may be attributed to the fully turbulent flow assumption. The development of the leading-edge suction then drives the lift towards the steady-state values. However, the low pressure aft of the midchord on the upper surface delays the recovery process until $\alpha = 5$ deg is reached.

The drag coefficient experiences a similar rapid increase with the development of the leading-edge vortex and the simultaneous collapse of the leading-edge suction. The increase in the drag coefficient is almost fivefold. The time history of the moment coefficient also follows the development of the flow closely. As the leading-edge suction grows, the nose-down pitching moment increases slowly. The suction associated with the leading-edge vortex and its downstream travel increases the nose-down pitching moment drastically, which leads to the moment stall. Following the leading-edge vortex, the suction induced by the trailing-edge vortex causes another indentation along the return cycle at $\alpha \cong 20$ deg ↓. At $\alpha \cong 10$ deg ↓, as the leading-edge suction redevelops while the

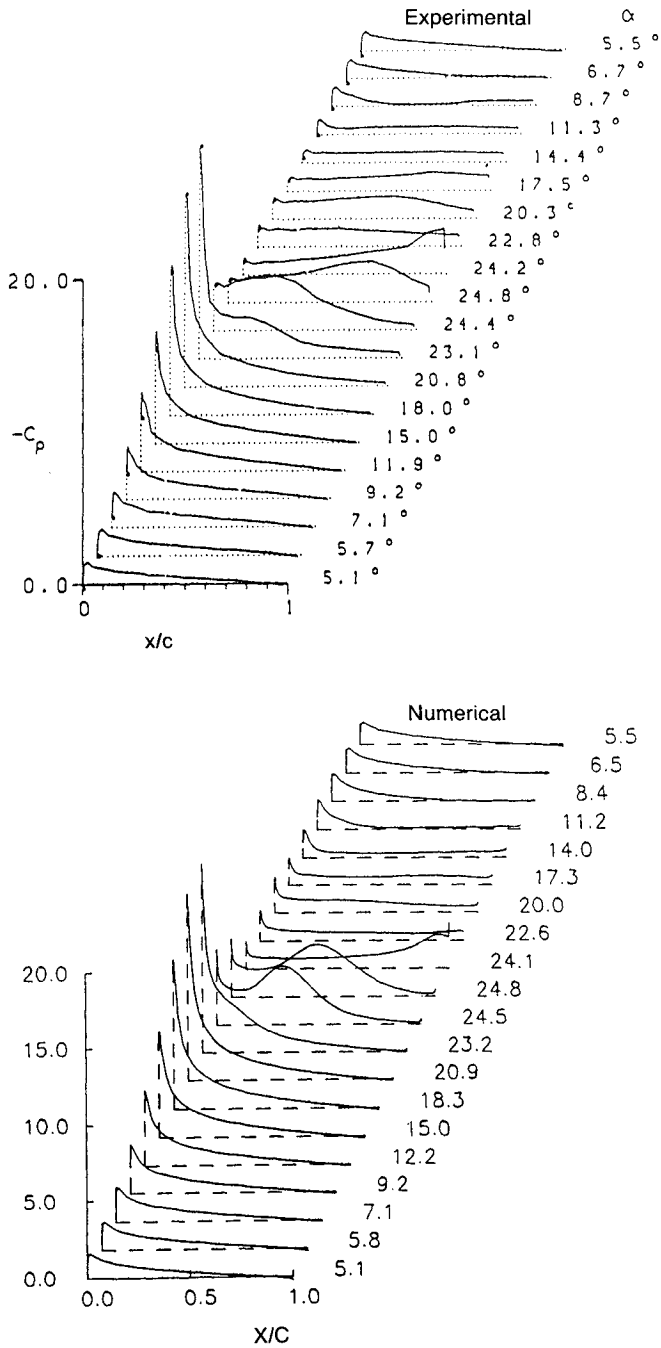

Fig. 6 Pressure distributions on upper surface: $\alpha_{min} = 5$ deg, $\alpha_{max} = 25$ deg, $Re = 10^6$, and $k = 0.15$.

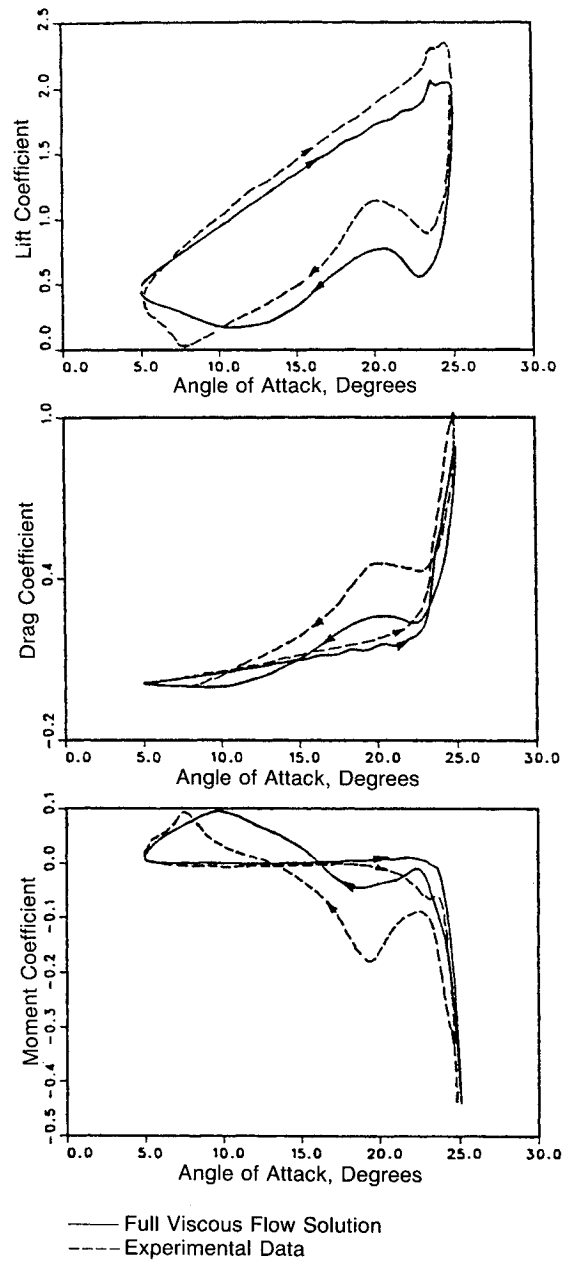

Fig. 7 Dynamic stall hysteresis loops: $\alpha_{min} = 5$ deg, $\alpha_{max} = 25$ deg, $Re = 10^6$, and $k = 0.15$.

flowfield over the downstream half of the airfoil is still separated, the moment coefficient reaches its maximum.

For the cases $k = 0.10$ and 0.25, the computed flowfields reveal the sequence of events similar to those observed in the case $k = 0.15$. These events include the flow reversal starting from the trailing edge, the formation of the leading-edge vortex, its downstream convection and shedding into the wake, and the formation of the trailing-edge vortex. However, different reduced frequencies cause the events to occur at

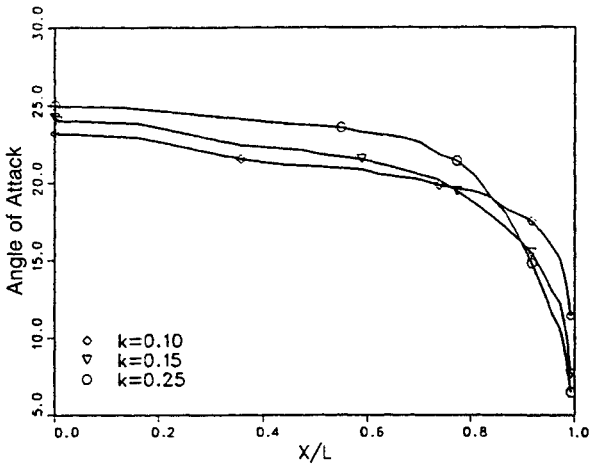

Fig. 8 Upstream propagation of reversed flow region: $\alpha_{min} = 5$ deg, $\alpha_{max} = 25$ deg, and $Re = 10^6$.

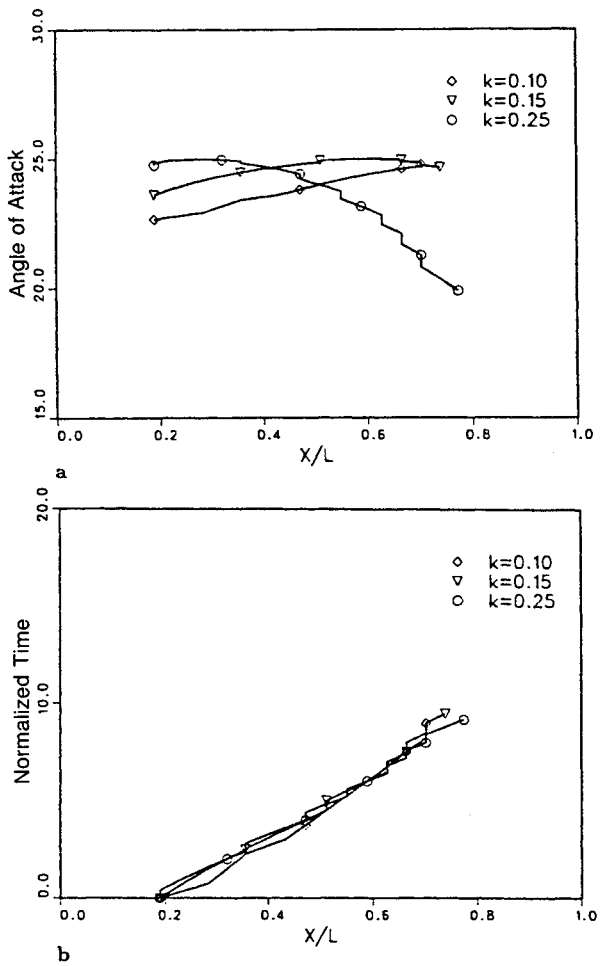

Fig. 9 Downstream propagation of leading-edge vortex suction peak: $\alpha_{min} = 5$ deg, $\alpha_{max} = 25$ deg, and $Re = 10^6$.

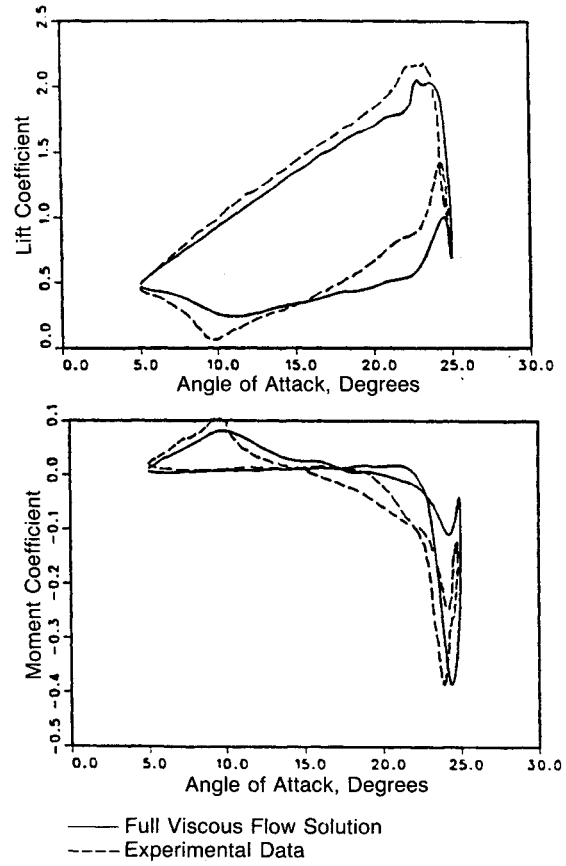

Fig. 10 Dynamic stall hysteresis loops: $\alpha_{min} = 5$ deg, $\alpha_{max} = 25$ deg, $Re = 10^6$, and $k = 0.10$.

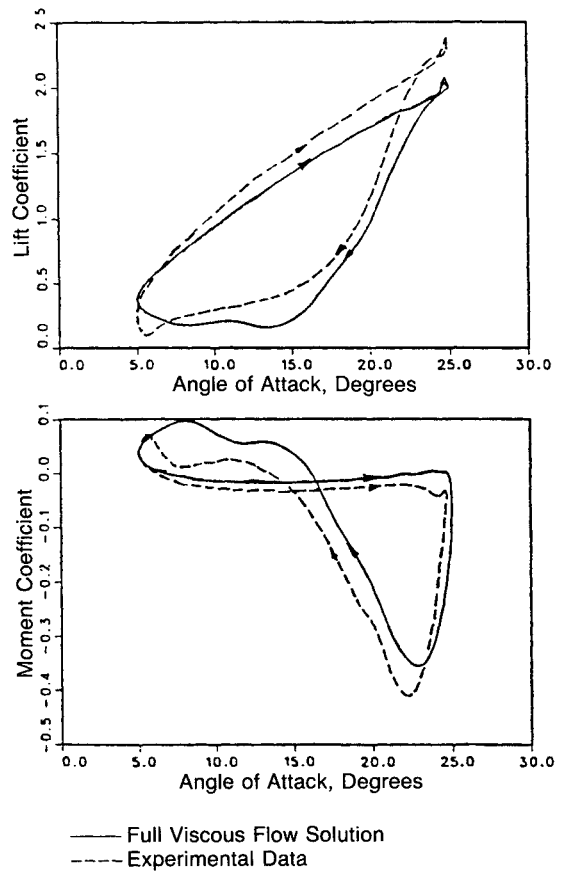

Fig. 11 Dynamic stall hysteresis loops: $\alpha_{min} = 5$ deg, $\alpha_{max} = 25$ deg, $Re = 10^6$, and $k = 0.25$.

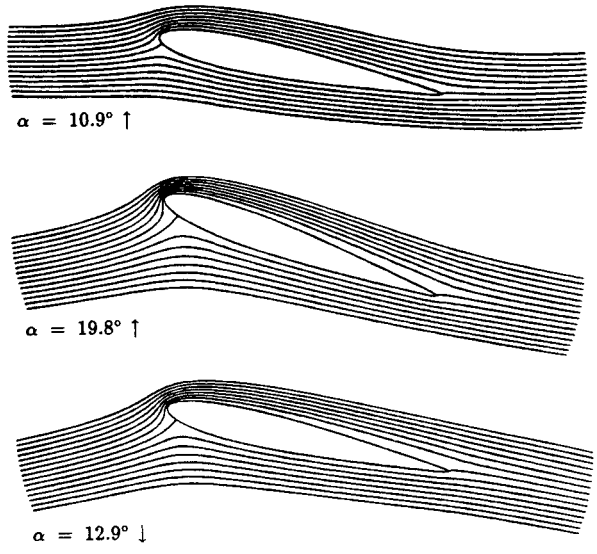

Fig. 12 Instantaneous streamlines: $\alpha_{min} = 0$ deg, $\alpha_{max} = 20$ deg, $Re = 1.5 \times 10^6$, and $k = 0.25$.

different angles of attack during the oscillatory motion, and as a result, the aerodynamic loading differs significantly.

In Fig. 8, the upstream propagation of the reversed flow region for the three different reduced frequencies is plotted with respect to the angle of attack. It is observed that as the reduced frequency increases, the flow reversal originates at a smaller angle of attack. In Figs. 9a and 9b the downstream convection of the leading-edge vortex that is assessed by tracing the suction peak associated with the vortex is shown. In Fig. 9b, the dimensionless time based on c/U_∞ is set to zero when the flow reversal is detected at the trailing-edge region. It is observed that as the reduced frequency increases, the formation of the leading-edge vortex occurs at a higher angle of attack. The propagation of the suction peak terminates when the peak cannot be detected any longer. This occurs as the vortex leaves the airfoil surface and sheds into the wake. The delay in the shedding of the vortex is significant in the case $k = 0.25$. However, Fig. 9b clearly shows that once the leading-edge vortex forms, the convection speed it consequently assumes is almost constant and independent of the reduced frequency in the range studied.

Aerodynamic load histories for the cases $k = 0.10$ and 0.25 are given in Figs. 10 and 11. As it is seen, the lift stall in case of $k = 0.10$ occurs at a lower incidence angle compared to that in the case of $k = 0.15$. Yet, in both cases the stall occurs during the upstroke before the maximum angle of attack is reached. In the case of $k = 0.25$ the growth of the leading-edge vortex and the associated rapid rise in the lift continues into the beginning phase of the downstroke. The bursting of the vortex and the drastic decrease of the lift occur during the downstroke. This sequence of events produces a small loop in the maximum lift region instead of spikes seen in cases $k = 0.10$ and 0.15. The influence of the trailing-edge vortex on the aerodynamic loads is also less pronounced in the $k = 0.25$ case.

Experimental investigations have shown that in some cases with sufficiently high reduced frequencies, the dynamic stall phenomenon can be prevented even though the static stall angle is substantially exceeded. The unsteady flowfield of such a case, with $\alpha_{min} = 0$ deg, $\alpha_{max} = 20$ deg, $k = 0.25$, and $Re = 1.5 \times 10^6$ computed using the full viscous flow analysis, is shown in Fig. 12. Although the flowfield seems to be fully attached along the motion, the investigation of the vorticity

Fig. 13 Instantaneous locations of wake vortex filaments: $\alpha_{min} = 0$ deg, $\alpha_{max} = 20$ deg, and $k = 0.25$.

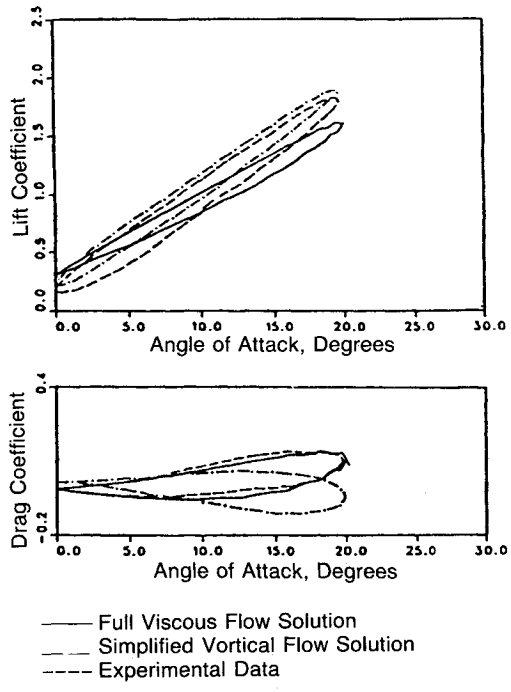

Fig. 14 Lift and drag hysteresis loops: $\alpha_{min} = 0$ deg, $\alpha_{max} = 20$ deg, $Re = 1.5 \times 10^6$, and $k = 0.25$.

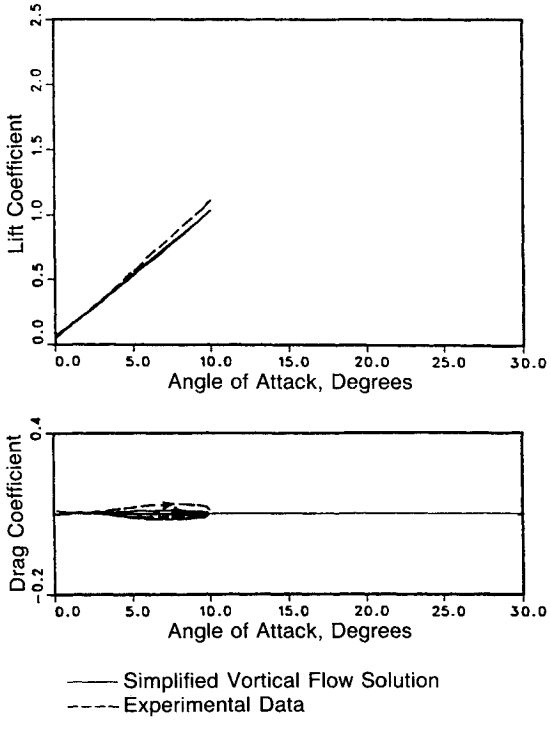

Fig. 15 Lift and drag hysteresis loops: $\alpha_{min} = 0$ deg, $\alpha_{max} = 10$ deg, and $k = 0.10$.

field reveals the presence of a very shallow reversed flow region forming at $\alpha \cong 9$ deg ↑ and extending up to the mid-chord at the maximum angle of attack.

The same flowfield is also computed using the simplified vortical flow analysis. The trailing vortex filaments in the wake that are represented by small circles of variable diameter are seen in Fig. 13. The size of the circles is proportional to the strength of the vortex filament. As it is observed, the trajectory of the vortex filaments is smooth while their magnitudes experience an oscillatory behavior in time. Since a uniform time step is employed, vortex filaments with the maximum strengths are shed when the pitching velocity is the maximum.

The aerodynamic load histories are given in Fig. 14. The computed aerodynamic loads are for the second cycle of the oscillatory motion. Although the agreements with experimental data are good, the simplified vortical flow analysis, which does not account for the thickening of the boundary layers and flow reversal, seems to agree better. This behavior may suggest that the uncertainty in the experiments is inclined towards measuring the normal force higher.

Figure 15 shows the aerodynamic load history computed by the simplified vortical flow analysis for the oscillatory motion of $\alpha_{min} = 0$ deg, $\alpha_{max} = 10$ deg, and $k = 0.10$. The prediction of the lift variation is remarkably good, whereas the drag is underpredicted along the upstroke. This simplified analysis, which neglects the boundary-layer thickness, might predict higher leading-edge suction, which would cause the drag to be predicted less. On the other hand, the negative drag, i.e., thrust, which is observed during the downstroke and predicted numerically as well, may be explained by the presence of the high suction at the leading edge whereas the suction on the upper airfoil surface is less than it was during the upstroke. This low suction on the upper surface is due to the apparent mass effect.

Concluding Remarks

The unsteady flowfields around large amplitude oscillating airfoils have been simulated numerically by two different yet closely related formulations. The computed unsteady flowfields and aerodynamic loads for the cases presented in this paper agreed well with the experimental data. Massive recirculating regions, the formation and convection of large vortex structures, and details of the dynamic stall phenomenon have been identified and their relationships to the flow parameters such as the reduced frequency and their maximum angle of attack have been assessed.

The full viscous flow analysis of the NACA 0012 airfoil has shown that the dynamics of the leading-edge vortex has a dominant effect on the dynamic stall behavior. As the reduced frequency of the oscillatory motion increases, the formation of the leading-edge vortex delays until higher angles of attack are reached. Once the leading-edge vortex forms, although it travels downstream with an almost constant speed, its initial formation determines the course of aerodynamic loads hysteresis loops. Distinguishing features of the loops are associated with different reduced frequency motions.

The accuracy and the efficiency of the full viscous flow analysis suggest that the computational method presented in this paper is well suited for unsteady aerodynamic analysis involving large amplitude motions of lifting bodies. This method can be employed practically for parametric studies of pitching airfoils undergoing dynamic stall phenomena. For attached flowfields, the simplified vortical flow analysis can be employed efficiently in predicting the unsteady lift. It is a valuable tool in research and preliminary design.

Acknowledgment

This work was supported by the Air Force Office of Scientific Research and the Army Research Office.

References

[1]Johnson, W., and Ham, N. D., "On the Mechanism of Dynamic Stall," *Journal of American Helicopter Society*, Vol. 17, Oct. 1972, pp. 36–45.

[2]McCroskey, W. J., Carr, L. W., and McAlister, K. W., "Dynamic Stall Experiments on Oscillating Airfoils," *AIAA Journal*, Vol. 14, No. 1, 1976, pp. 57–63.

[3]Ericsson, L. E., and Reding, J. P., "Dynamic Stall at High Frequency and Large Amplitude," *Journal of Aircraft*, Vol. 17, No. 3, 1980, pp. 136–142.

[4]Mehta, U. B., "Dynamic Stall of an Oscillating Airfoil," Paper 23, *Unsteady Aerodynamics*, AGARD CP-227, Sept. 1977.

[5]Carr, L. W., McAlister, K. W., and McCroskey, W. J., "Analysis of the Development of Dynamic Stall Based on Oscillating Airfoil Experiments," NASA-TN-D-8382, 1977.

[6]McCroskey, W. J., McAlister, K. W., Carr, L. W., and Pucci, S. L., "An Experimental Study of Dynamic Stall on Advanced Airfoil Sections," NASA TM-84245, Vol. 1, July 1982.

[7]McAlister, K. W., Pucci, S. L., McCroskey, W. J., and Carr, L. W., "An Experimental Study of Dynamic Stall on Advanced Airfoil Sections, Pressure and Force Data," NASA TM-84245, Vol. 2, Sept. 1982.

[8]McCroskey, W. J., "The Phenomenon of Dynamic Stall," NASA TM-81264, Mar. 1981.

[9]Sankar, N. L., and Tang, W., "Numerical Solution of Unsteady Viscous Flow Past Rotor Sections," AIAA Paper 85-0129, Jan. 1985.

[10]Wu, Jiunn-Chi, "A Study of Unsteady Turbulent Flow Past Airfoils," Ph.D. Thesis, School of Aerospace Engineering, Georgia Institute of Technology, Atlanta, GA, June 1988.

[11]Wu, J. C., "Theory for Aerodynamic Force and Moment in Viscous Flows," *AIAA Journal*, Vol. 19, No. 4, 1981, pp. 432–441.

[12]Wu, J. C., Wang, C. M., and Gulcat, U., "Zonal Solution of Unsteady Viscous Flow Problems," AIAA Paper 85-0034, Jan. 1985.

[13]Wu, J. C., Wang, C. M., and Tuncer, I. H., "Unsteady Aerodynamics of Rapidly Pitched Airfoils," AIAA Paper 86-1105, May 1986.

[14]Wu, J. C., and Tuncer, I. H., "A Unified Theoretical-Computational Method for Viscous Unsteady Rotor Aerodynamics," 44th Annual Forum and Technology Display Proceedings, American Helicopter Society, Washington DC, June 1988.

[15]Wu, J. C., "Numerical Boundary Conditions for Viscous Flow Problems," *AIAA Journal*, Vol. 14, No. 8, 1976, pp. 1042–1049.

[16]Baldwin, B. S., and Lomax, H., "Thin Layer Approximation and Algebraic Model for Separated Flows," AIAA Paper 78-0257, Jan. 1978.

[17]Wang, C. M., Wu, J. C., and Tuncer, I. H., "Accurate Determination of Surface Pressure in High Reynolds Number Flows," First International Conference on Computational Methods in Flow Analysis, Sept. 1988.

[18]Wang, C. M., and Wu, J. C., "Numerical Solution of Navier-Stokes Problems Using Integral Representations with Series Expansions," AIAA Paper 85-0034, Jan. 1985.

[19]Tuncer, I. H., "Unsteady Aerodynamics of Oscillating and Rapidly Pitched Airfoils," Ph.D. Thesis, School of Aerospace Engineering, Georgia Institute of Technology, Atlanta, GA, Aug. 1988.